Experimental Pig Model of Old Myocardial Infarction with Long Survival Leading to Chronic Left Ventricular Dysfunction and Remodeling as Evaluated by PET

Noboru Teramoto[1], Kazuhiro Koshino[1], Ikuo Yokoyama[2,3], Shigeru Miyagawa[4], Tsutomu Zeniya[1], Yoshiyuki Hirano[1], Hajime Fukuda[1], Junichiro Enmi[1], Yoshiki Sawa[4], Juhani Knuuti[5], and Hidehiro Iida[1]

[1]Department of Investigative Radiology, National Cerebral and Cardiovascular Center Research Institute, Osaka, Japan; [2]School of Medicine and Faculty of Medicine, The University of Tokyo, Tokyo, Japan; [3]Department of Cardiovascular Medicine, Sanno Hospital, International University of Health and Welfare, Tokyo, Japan; [4]Department of Cardiac Surgery, Osaka University, School of Medicine, Osaka, Japan; and [5]Turku PET Centre, University of Turku, Turku, Finland

A pig model of reduced left ventricular (LV) function and remodeling or chronic heart failure with long survival after myocardial infarction (MI) has not been established. The aim of this study was to evaluate the pathophysiologic status of a pig model of old MI using a series of PET studies. **Methods:** Twenty-seven male farm pigs were divided into 2 groups: 7 animals in the control group and 20 animals that underwent a proximal coronary artery (CA) occlusion using an ameroid constrictor after distal CA ligation. A series of PET examinations was performed to assess LV volumes, LV functions, myocardial perfusion response to adenosine, and viability as water-perfusable tissue index. **Results:** The distal CA ligation inhibited arrhythmia during and after the operation, and a transmural anteroseptal MI, with an infarction area of 27% ± 5% of the whole left ventricle, was generated with a survival rate of 75% at 4 mo. Wall motion evaluated by ^{18}F-FDG PET was diffusely reduced, including the noninfarcted wall. Global LV ejection fraction as assessed by gated C^{15}O PET was reduced (39% ± 16%) in the group undergoing occlusion, compared with the control group (66% ± 16%, $P < 0.05$). LV end-systolic (31.4 ± 9.2 cm^3) and end-diastolic (52.7 ± 10.2 cm^3) volumes were increased, compared with controls (15.2 ± 9.4 cm^3, $P < 0.01$, and 41.7 ± 11.5 cm^3, $P < 0.05$, respectively). Histology showed hypertrophy and development of microscopic fibrosis in noninfarcted myocardium. PET demonstrated the reduced myocardial perfusion response to adenosine and also reduced water-perfusable tissue index in remote segments. **Conclusion:** The pig model of old MI generated by the chronic proximal CA obstruction after distal ligation was characterized by LV dysfunction and remodeling, with a high survival rate.

Key Words: experimental model; PET; myocardial flow reserve; remodeling; regeneration therapy

Chronic heart failure (CHF) is an increasing health concern (*1*). Myocardial infarction (MI) is the cause of CHF in two thirds of the patients, and the morbidity and mortality remain high (*2,3*). The potential therapies, such as new class of pharmacologic agents and cell therapy (*4*), need to be tested in proper animal models to demonstrate the effects and outcome before initiating clinical trials. Dogs have been extensively used in heart research. Because the coronary arterial systems in dogs can develop collaterals quickly when myocardial ischemia occurs, it has been difficult to produce a large MI that typically introduces CHF with general characteristics of left ventricular (LV) remodeling (*5*).

Pigs have been considered better suited than dogs for pathophysiologic research of ischemic heart diseases, because the coronary system of pigs is more similar to that of humans (*6*). Tolerance of ischemia and denervation after ischemia in pigs is also similar to that in humans (*6*). Because of the delayed development of collaterals after occlusion, ligation of a peripheral part of the coronary arterial system generates a small MI (*7*). However, an experimental model of large MI introducing global LV dysfunction is difficult to develop, because sudden cardiac death (SCD) due to fatal arrhythmias and an intolerance of ischemia frequently occurs in pigs (*8*). The models of small MI made by the ligation of a peripheral part of the coronary arterial system demonstrate reasonably good survival rates but only for a small infarction. The model of small MI using a coronary ameroid constrictor (model MRI-2.50-TI; Research Instruments SW) has also demonstrated moderate SCD rates (*6,8–13–15*), but the animals develop primarily chronic ischemia or hibernating myocardium, without a significant amount of scar tissue. Thus, the limitations of current models are that the infarcted region is small and that the hearts are not developing a clinical picture of CHF with global LV dysfunction, LV dilatation, and remodeling.

On the other hand, Shen et al. (*16*) developed an experimental pig model of MI and heart failure. Sequential

ligation of distal and proximal coronary arteries was used to establish MI with a reasonable survival rate, and pacing tachycardia was used to achieve heart failure. However, this pig model was studied over only a short term (21 d) and required pacing tachycardia to cause CHF. There has been little evaluation of pathophysiology and no evidence of the presence of cardiac remodeling.

This aim of this study was to characterize the pig model of old MI. We first reinvestigated the technique of generating a pig model of relatively large MI causing global LV dysfunction and LV remodeling in segments remote from the infarcted region, by means of the sequential ligation of distal and proximal coronary arteries without the pacing procedures. We then evaluated the pathophysiologic characteristics of this animal model by comprehensively analyzing histology, LV volumes and LV function, myocardial perfusion response to adenosine, and perfusable tissue fractions (PTF) in the remote segment, using an advanced PET technique.

MATERIALS AND METHODS

Subjects

Male farm pigs, 3 mo old at the start of the study (weight range, 18–23 kg; mean weight ± SD, 20 ± 1.2 kg), were used. The animals were divided into 2 groups. Group A consisted of 7 pigs without any operation and was designated as the control group (average body weight, 26 ± 2.4 kg). Group B consisted of 20 pigs that underwent occlusion using an ameroid constrictor (7); ligation of the distal left anterior descending coronary artery (LAD) was performed before the ameroid constrictor was used. Of the 16 pigs that survived for 4 mo after the operation, 7 underwent PET studies. The other 9 were assigned to tissue-regenerative projects. The average body weight of this group of 7 pigs was 42 ± 8.2 kg at the time of the PET scan.

Animals were maintained and handled in accordance with guidelines for animal research (17). The study protocol was approved by the local Committee for Laboratory Animal Welfare, National Cardiovascular Center, Osaka, Japan.

Permanent Occlusion Procedures

[Fig. 1] In group B, permanent occlusion was made at the proximal LAD using an ameroid constrictor (18) (Fig. 1) as follows. Pigs were preanesthetized by an intramuscular injection of ketamine hydrochloride (20 mg/kg; Ketaral [Diichi-Sankyo]) and xylazine hydrochloride (2 mg/kg; Celactal [Bayer HealthCare]). The animals were positioned supine, and a 22-gauge indwelling needle (Surflo F&F; Terumo) was inserted in the central vein of the auricle. A 3-way cock (Terufusion TS-TR2K; Terumo) was attached to the external cylinder of the indwelling needle and connected for continuous anesthetic injection. The animals were intubated with an endotracheal cannula (6 French; Sheridan) and then connected to an artificial respirator (Single Animal Volume Controlled Ventilators model 613 [Harvard Apparatus]) with a stroke volume of 200–300 cm³/stroke and frequency of 20/min. Propofol (6 mg/kg/h; Diprivan [Astra-Zeneca]) and vecuronium bromide (0.05 mg/kg/h; Musculux [Sankyo Yell Yakuhin Co., Ltd.]) were continuously infused using a syringe pump (Terufusion TE-3310N; Terumo). Then, the animals were fixed in a recumbent position so that the left thorax was exposed, and the outer layer of skin and muscles between the third and fourth ribs was dissected. The distance between the third and fourth ribs was widened with a rib spreader to allow a direct view of the left auricle and LAD. The pericardium was dissected along the LAD, from the upper part of the left auricle (~6 cm), to expose the myocardium around the LAD. The LAD on the proximal side, below the left auricle from the myocardium, was exfoliated for approximately 1 cm. A lidocaine hydrochloride jelly (Xylocaine jelly; Astra-Zeneca) was applied to anesthetize the area.

A complete ligation was first made on the distal LAD (no. 9), immediately after the second diagonal branch, using a suture (2-0; Nescosuture) approximately 20 min before the ameroid constrictor was fastened. An ameroid constrictor (COR-2.50-SS; Research Instruments) was then fastened using sutures as displayed in Figure 1. To enhance the effect of the ameroid constrictor, 2 additional suture strings were loosely rounded at the site of the ameroid so that these strings were located between (below) the ameroid constrictor and arterial wall.

PET Procedures

After fasting overnight, the pigs were sedated with ketamine hydrochloride (20 mg/kg) and xylazine hydrochloride (2 mg/kg) by intramuscular injection. Anesthesia was induced and maintained with intravenous propofol (6 mg/kg/h) and vecuronium bromide (0.05 mg/kg/h). The animals were intubated and mechanically ventilated with a mixture of 25% oxygen and 75% nitrogen at 10 mL/kg plus 50 mL/stroke at 20 strokes/min. Catheters were placed in the femoral artery to monitor the arterial blood pressure and in the femoral vein to infuse $H_2^{15}O$ or ^{18}F-labeled FDG. Systolic and diastolic blood pressure, heart rate, and arterial blood gases were monitored.

A series of PET scans was obtained using an ECAT-HR tomograph (CTI Inc.). The blood-pool images were obtained after the animals inhaled 2.7 GBq of $C^{15}O$ gas (19). Arterial blood samples were taken every minute during the $C^{15}O$ scan, and their radioactivity concentration in the whole blood was measured. Additional electrocardiogram-gated $C^{15}O$ images were obtained (16 gates). After 12–15 min of ^{15}O radioactivity decay, 7 dynamic $H_2^{15}O$ PET scans were acquired at intervals of 12–15 min. The first and the last scans were obtained without pharmacologic stress, and the second through sixth scans were obtained during intravenous infusion of adenosine (100, 200, 400, 600, and 800
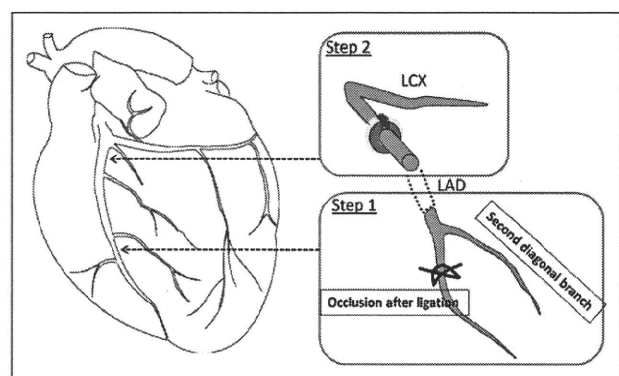
FIGURE 1. Ligation of LV LAD. Distal LAD after second diagonal branch was ligated, and 30 min later ameroid constrictor was placed at proximal LAD. Two suture strings were inserted between ameroid constrictor and arterial wall to make occlusion complete. LCX = left circumflex artery.

[only for group A] μg/kg/min). The 6-min dynamic scan of 26 frames (12 × 5, 8 × 15, and 6 × 30 s) was started when radioactivity appeared in the right ventricle. Furthermore, another PET scan using ^{18}F-FDG was acquired using a euglycemic hyperinsulinemic clamp (20,21). For this study, insulin (4 mIU/kg/h) and glucose (5–8 mg/kg/min) were continuously infused over 2 h, and then approximately 111 MBq of ^{18}F-FDG was intravenously injected. The blood glucose was 109 ± 10.6, 105 ± 3.8, and 107 ± 10.0 mg/dL at the time of ^{18}F-FDG injection. PET images were acquired dynamically for 60 min, and the images acquired during the last 30 min were used for further analysis. An additional electrocardiogram-gated scan was obtained for 30 min to estimate myocardial wall motion and wall thickening.

After the PET scans, coronary angiography was undertaken to confirm the occlusion of LAD. A portable angiographic camera (Digital Mobile Imaging System OEC Series 9800; GE Healthcare U.K. Ltd.) was used with the contrast medium (Omnipaque 300; Daiichi-Sankyo).

Histologic Analysis

At the end of the study, pentobarbital sodium was administered, and animals were euthanized. The animals' hearts were then excised and sliced at a thickness of 10 mm to correspond to PET images (22). The slices were stained with Masson trichrome and hematoxylin and eosin. The surface area of the infarcted LV wall on the stained slices was calculated according to a previously describe procedure (22). The length of the infarcted zone, including both transmural and nontransmural infarction, was measured on each of the stained slices along the LV wall. The defect surface area was then calculated as a summation of the defect length multiplied by the slice interval. The cell and microvascular structures were also analyzed. In particular, development of fibrosis, cell enlargement, and degeneration of the vascular network were visually estimated. The analysis was masked from the other analyses.

Data Analysis

The extravascular tissue density images (g/mL) were calculated by subtracting the C[15]O blood volume from the transmission images (23). The relative images of myocardial blood flow (MBF) and water-PTF (g/mL) were also generated from the dynamic H$_2$[15]O images (22,23). The relative accumulation of ^{18}F-FDG was calculated using validated techniques (24). The regions of interest were placed in the anterior wall and lateral–anterior wall, which corresponded to the MI and normal-tissue regions, respectively. The regions of interest were then copied to other images, and the quantitative parameters of regional MBF (mL/min/g), PTF (g/mL), and arterial blood volume V$_a$ (mL/mL) were calculated using nonlinear least-squares fitting as described previously (22,23). These calculations were done for all H$_2$[15]O PET studies to estimate baseline MBF and the adenosine-based responses both in MI and in non-MI regions.

The water-perfusable tissue index (PTI) (23,25,26), which was defined as the fraction of water-perfusable tissue over total tissue, was calculated by dividing PTF by the extravascular tissue density images. This calculation was done for each myocardial region and compared between the infarcted anterior wall and normal posterior–lateral wall regions. The obtained values were also compared with control subjects.

The LV ejection fraction and cardiac output were evaluated by counting the total counts within the LV area from the typical electrocardiogram-gated C[15]O images shown in Figure 2. The wall motion was analyzed using electrocardiogram-gated ^{18}F-FDG images. The wall motion score was divided into 4 levels (normal, 0; hypokinetic, 1; akinetic, 2; and dyskinetic, 3) and defined for the anterior wall and contralateral (lateral–posterior) wall regions.

The surface area of the infarcted LV wall on the ^{18}F-FDG and PTF images was calculated as described previously (22). A significant defect was defined as a value less than 50% of that in the control region, which was defined in the contralateral region, indicating preserved ^{18}F-FDG, preserved PTF, and elevated MBF during adenosine. The myocardial midlines were then traced along the 50% of peak count boundary of the C[15]O blood volume images at each slice (22). The surface area of the defect was calculated as a summation of the defect length multiplied by the slice interval. These defect surface areas were compared with those obtained from the stained slices.
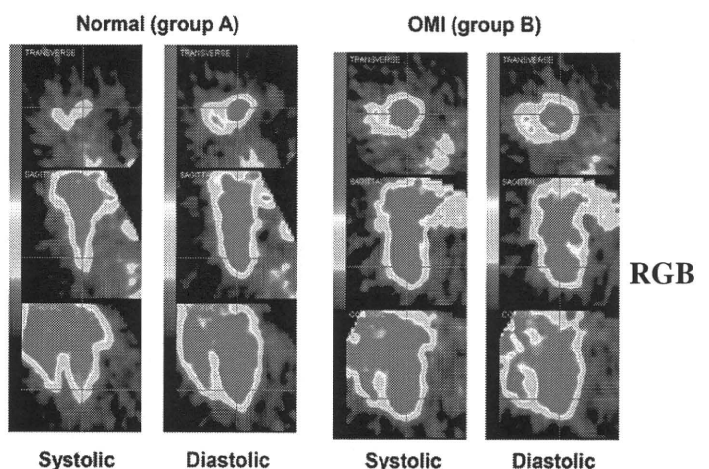
All data were presented as mean ± SD. Pearson correlation and linear regression analyses were used to evaluate relationships between the 2 values. A P value of less than 0.05 was considered statistically significant.
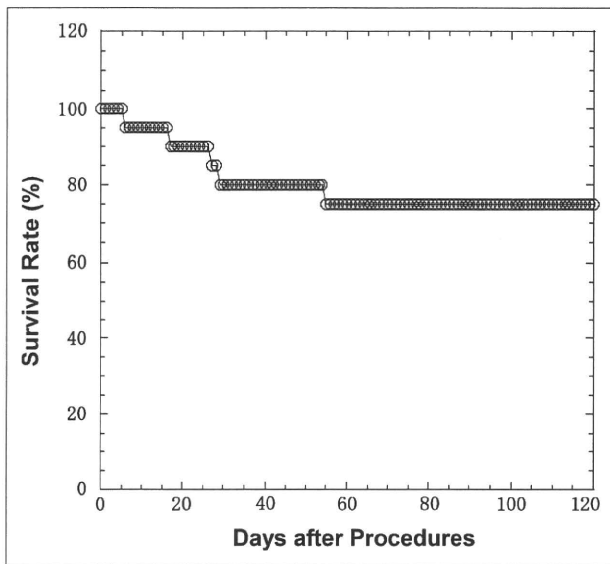
RESULTS

Survival Rates of Animal Groups

No adverse events were detected in group A; in group B, 4 pigs (20%) died within a month and an additional pig 1 mo after that. Thus, the total survival rate at 4 mo was 75% in group B. Severe arrhythmia occurred in all animals in group B during the operation. The arrhythmia and fibrillation, introducing the sudden cardiac death, were significantly suppressed at approximately 20 min after ligation of the distal LAD. Figure 3 displays the survival rates of the pigs that underwent the operation.

Of the pigs in group B that survived for 4 mo, 7 were selected for further characterization and imaging studies. These 7 animals were compared against the animals in group A, on which no operation was performed. The characteristics of the 2 groups at the time of the imaging

FIGURE 2. Typical images obtained from electrocardiogram-gated PET scans with C[15]O inhalation at end-systolic and end-diastolic phases. OMI = old MI.

FIGURE 3. Survival rates for group B after ameroid constrictor was placed.

significantly increased (31.4 ± 9.2 cm³ in group B vs. 15.2 ± 9.4 cm³ in group A, $P < 0.01$), and LV end-diastolic volume was also significantly increased (52.7 ± 10.2 cm³ in group B vs. 41.7 ± 11.5 cm³ in group A, $P < 0.05$). Increased end-systolic and end-diastolic volumes are also clearly visible in Figure 2. Systolic blood pressure and diastolic blood pressure, as well as rate–pressure product, were reduced during adenosine study in both groups. Heart rate was increased in group A but not in group B. Other parameters such as hemoglobin concentration (g/dL), percentage saturation of arterial O_2, $PaCO_2$ (mm Hg), and PO_2 (mm Hg) were not significantly different between the 2 groups. Table 2 shows detailed hemodynamic parameters [Table 2] and the results from the histologic analysis for each individual animal in group B. Wall motion score was reduced (akinesis–dyskinesis or 2–3) in the anterior wall, which includes the area of MI. The wall motion score was also reduced diffusely in all animals and indicated hypokinesis (grade 1) in the infarct-remote posterolateral wall. The coronary angiography demonstrated complete occlusion of the LAD in all animals in group B. As shown in Figure 4, no [Fig. 4] clear collateral circulation existed.

Imaging Results

The myocardial perfusion ($H_2^{15}O$) and metabolism (^{18}F-FDG) images at the mid ventricular plane and their corresponding slices after histochemical staining for the animals in group B are displayed in Figure 5. In all animals, clear [Fig. 5] signs of MI were detected in the anterior wall. The surface area of the MI was 13.7 ± 4.3 cm², which corresponded to 27% ± 9% of the whole left ventricle. Both PTF and ^{18}F-FDG images visually agreed well with the stained slices. Moreover, the ^{18}F-FDG images agreed well with the qualitative PTF images in all animals. The spatial distribution and size of the developed MI are visually reproducible

[Table 1] studies are displayed in Table 1. Because the animals in group B were allowed to grow after operation, they were larger at the time of the imaging studies.

Characteristics of Groups

Table 1 shows the hemodynamic data for the animals in groups A and B. Compared with group A, group B showed a significantly reduced heart rate and diastolic blood pressure and, thus, rate–pressure product. In addition, the global LV ejection fraction measured with gated $C^{15}O$ PET in group B was significantly reduced (39% ± 16% [24%–59%] in group B vs. 66% ± 16% [46%–91%] in group A, $P < 0.01$). LV end-systolic volume in group B was

TABLE 1
Physiologic Parameters of Pigs at Time of PET

Parameter	Group A (control, $n = 7$)	Group B (old MI, $n = 7$)
Body weight (kg)	26 ± 2.4	41 ± 8.2
Heart rate (beats·min⁻¹)	72 ± 22.4 (82 ± 21.4*)	52 ± 6.3† (53 ± 9.2)
Systolic blood pressure (mm Hg)	131 ± 22.1 (95 ± 22.4‡)	111 ± 18.3† (97 ± 15.0*)
Diastolic blood pressure (mm Hg)	92 ± 19.3 (49 ± 16.7‡)	74 ± 13.6† (57 ± 11.9‡)
Rate pressure product (mm Hg·min⁻¹)	9,567 ± 3,616 (5,657 ± 3201‡)	5,732 ± 1,151† (4,445 ± 948*)
Wall thickness (posterior–lateral wall) (cm)	1.2 ± 0.1	1.6 ± 0.1‡
End-diastolic LV volume (mL)	41.7 ± 11.5	52.73 ± 10.2†
End-systolic LV volume (mL)	15.2 ± 9.4	31.4 ± 9.2*
LV ejection fraction (%)	66.0 ± 16.2	39.7 ± 16.9*
Hemoglobin concentration (g/dL)	13 ± 1.5	12 ± 0.9
Saturation of arterial O_2 (%)	99 ± 1.0	99 ± 0.6
pCO_2 (mm Hg)	39 ± 2.7	41 ± 2.8
pO_2 (mm Hg)	125 ± 20.1	141 ± 11.4

*$P < 0.01$.
†$P < 0.05$.
‡$P < 0.001$.
Data are mean ± SD. Values in parentheses are from administration of maximum dose of adenosine.

jnm084848-pm ■ 4/15/11

TABLE 2
Hemodynamic Parameters of Pigs with Old MI (Group B)

Subject no.	BW (kg)	HR (beats·min⁻¹)	SBP (mm Hg)	DBP (mm Hg)	RPP (mm Hg·min⁻¹)	tHb (g/dL)	SAT (%)	pCO₂ (mm Hg)	pO₂ (mm Hg)	WM Anterior wall	WM Posterior-lateral wall	WT (posterior-lateral wall)	EDV (mL)	ESV (mL)	EF (%)	LV surface area (cm²)	MI surface area (cm²)	DAF (%)
1	37	53	117	72	6,201	10.8	98.7	37.8	132	3	1	1.6	39.5	29.9	24.3	53.7	10.9	20.3
2	39	38	110	70	4,180	11.5	98.9	37	154.5	2	1	1.6	58.2	42.4	27.1	57	16.2	28.4
3	33	53	85	60	4,505	11.5	99.3	39.3	137.7	3	1	1.6	55.4	42.3	23.6	50	16	31.9
4	32	55	91	58	5,005	11.3	99.6	40.7	135.5	—	—	1.8	0	0	0	53.9	9.2	17.1
5	45	52	137	93	7,124	10.3	98.1	43.6	124.1	3	1	1.8	68.4	27.6	59.7	50	19.9	39.7
6	50	52	126	90	6,552	11.8	99.7	42.8	148.4	3	1	1.5	49.3	27.1	45	48.6	15.5	31.8
7	53	58	113	78	6,554	13.3	99	43.7	152.8	2	1	1.5	45.7	19.1	58.2	49.8	8.4	16.9
Mean	41	52	111	74	5,732	12	99	41	141	2.7	1	1.6	52.7	31.4	39.7	51.9	13.7	26.6
SD	8.2	6.3	18.3	13.6	1,151	0.9	0.6	2.8	11.4	0.5	0	0.1	10.2	9.2	16.9	3.05	4.3	8.7

BW = body weight; HR = heart rate; SBP = systolic blood pressure; DBP = diastolic blood pressure; RPP = rate–pressure product; tHB = hemoglobin concentration; SAT = saturation of arterial O₂; WM = wall motion; WT = wall thickness; EDV = end-diastolic LV volume; ESV = end-systolic LV volume; EF = ejection fraction; DAF = defect area fraction.

RGB
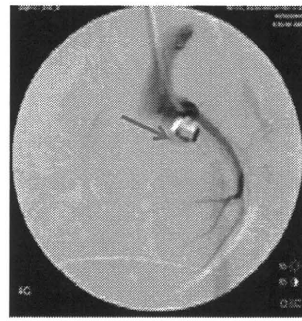
FIGURE 4. Example of coronary angiogram in animal with ameroid constrictor (arrow) (group B).

among the animals. Myocardial hypertrophy was visible in the wall regions remote from the infarcted area. In group B, the posterior–lateral wall thickness estimated from histochemical staining was 16 ± 1 mm (Table 2), which was significantly greater than that of group A (12 ± 1 mm; Table 1) ($P < 0.001$).

Further analysis of the size of the infarcted region is displayed in Figure 5B. We excluded 1 animal whose ^{18}F-FDG PET images demonstrated high accumulation at the anterior LV area (and therefore a smaller value in the defect surface area), which was attributed to the adhesion or inflammation between the myocardial and chest walls. Thus, the defect area on histology showed intersubject variation of approximately 20%. The results of both ^{18}F-FDG and PTF image analysis and histochemical analysis agreed well (Fig. 5B). Baseline and adenosine-stimulated MBF were also clearly blunted in the anterior wall in the animals in group B (Fig. 6A). Interestingly, abnormally [Fig. 6] reduced adenosine flow response also was detected in the myocardial regions remote from the MI in group B, whereas the baseline flow values were normal.

Further analysis of myocardial PTF and PTI values—indices of PTF—revealed that these values were significantly reduced in the infarcted anterior wall in group B (Fig. 6B). PTI was also moderately but significantly (~10%) reduced in the remote myocardial wall in group B.

Histologic Analysis

Histologic analysis did not show any signs of MI in group A, but transmural anterior wall MI was apparent in all animals in group B. Hypertrophy was detected in the posterior wall of group B in all animals. Multinuclear muscle cell breeding (Fig. 7A) and hyperplasia of blood [Fig. 7] vessels (Fig. 7B) were also visible in all animals in group B, mostly in the subendocardial regions. Denaturation necrosis with epicardial fibrous change and hypertrophy has also been seen in the lateral–posterior wall regions of group B (Fig. 7C).

DISCUSSION

This study demonstrated that 75% of pigs with old MI generated by the 2 steps of LAD ligation survived more than 4 mo. Such a long survival has never, to our

A PIG MODEL OF OLD MYOCARDIAL INFARCTION • Teramoto et al. **765**

FIGURE 5. (A) Histologic, PTF, and ^{18}F-FDG slices at middle level of left ventricle in 7 animals of group B. Spatial distribution and size of MI are visually reproducible among animals. Myocardial hypertrophy was visible in remote myocardial wall regions. (B) Comparison of defect surface areas obtained from histologic stained slices with PET images using ^{18}F-FDG and PTF. MTC = Masson trichrome.

RGB
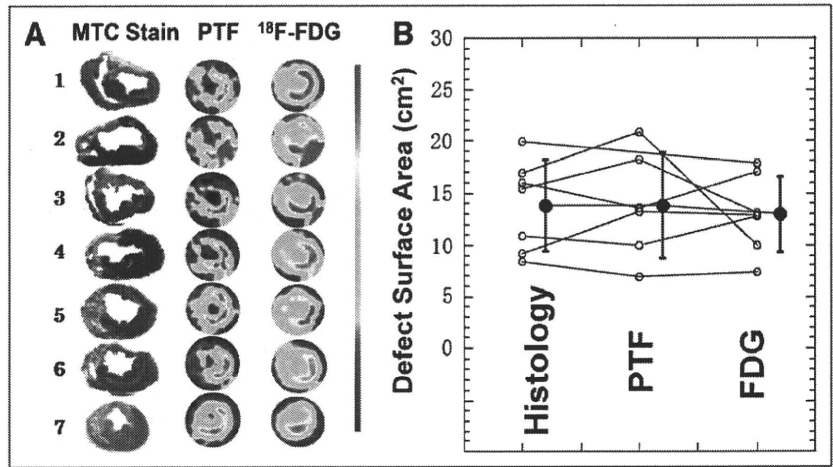
knowledge, been accomplished in any studies of pig heart disease. The size of MI reached approximately 27% of the whole left ventricle, causing the remodeling and global LV dilatation (significantly increased LV end-systolic and end-diastolic volumes) to be associated with reduced global LV function. PET with C^{15}O and ^{18}F-FDG showed that regional LV wall motion was impaired not only in the infarcted region but also in the myocardial areas remote from the MI. PET also demonstrated reduced MBF reactivity in remote regions in addition to the infarct area. PTI was also reduced in the remote region, suggesting development of microscopic fibrosis. Moreover, other findings from histology indicated the existence of abnormalities in the nonin-

farcted area remote from the MI. These results indicate that this animal model may be close to human CHF after MI.

Shen et al. (16) adopted additional pacing tachycardia in pigs after sequential coronary artery ligations and observed global LV dysfunction, claiming that CHF was introduced. The present study is similar to the study by Shen et al. (16) but is based on only sequential coronary artery obstructions accomplished with acute distal coronary artery occlusion followed by a chronic proximal coronary occlusion with an ameroid constrictor, causing similar LV dysfunction. Of note was the better survival rate (80% at 1 mo, 75% at 4 mo) demonstrated in the current report than in any previous report (6,8–12,14,16), including Shen et al.
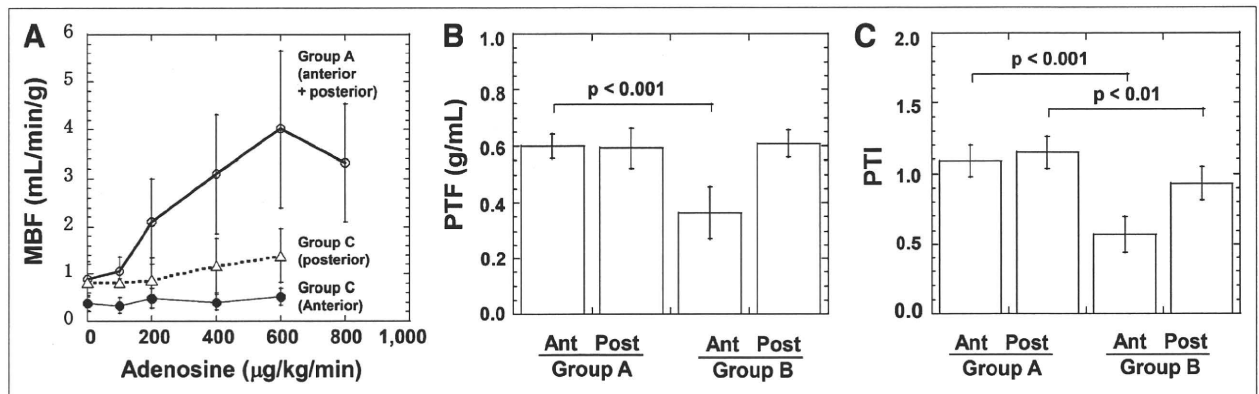
FIGURE 6. Results from PET studies. (A) Regional MBF as function of adenosine dose. In group A, MBF increases with increasing adenosine dose. In infarcted anterior wall of group B, MBF is reduced at rest and does not respond to adenosine. In posterior wall region, adenosine reactivity was significantly reduced. (B and C) Comparison of water-PTF (B) and water-PTI (C). Both were reduced in anterior wall of group B. PTI was also reduced in posterior wall in group B. Ant = anterior; Post = posterior.
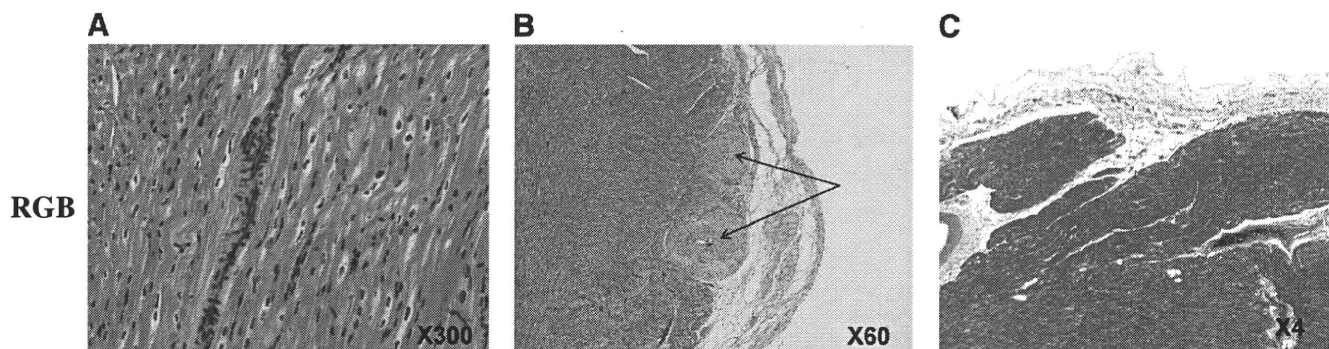
FIGURE 7. Typical images of histologic staining obtained from group B. Hypertrophy with multinuclear muscle cell breeding (A), hyperplasia of blood vessels shown as arrows (B), and denaturation necrosis often seen in subendocardial regions, as in this picture (C), are typical findings.

(73.3% at 21 d). In addition, it has not been confirmed whether such a good survival rate at 21 d could last more than 4 mo after producing global LV dysfunction with MI. Our preliminary experiment, independently performed on 69 farm pigs, demonstrated that when the proximal LAD was occluded by the ameroid constrictor alone, 45 pigs (65%) died within a month, and the total survival rate was 30% at 4 mo. This survival rate is significantly smaller than the rates from the present study.

The reason why animals with MI acquired such good survival is not fully understood. However, it was clearly observed that the ligation of the peripheral coronary artery before the gradual occlusion of the main trunk of the LAD apparently inhibited the fibrillation during the operation. This procedure is obviously effective at protecting against fatal arrhythmias. This preconditioning effect is supported by the experiments of Moses et al. (*27*), in which ischemic preconditioning of the distal coronary artery protected cardiac muscle through a mechanism involving the potassium channels of mitochondria and myocytes. There may be contributions from other preconditioning factors (*9,28–30*) that associate with increased tolerance of ischemia. Another mechanism could be associated with the modulation of sympathetic tone. It has been reported that regional heterogeneity in myocardial cellular mechanisms (responsible for myocardial cellular depolarization) and repolarization in hibernating myocardium (*12*) can induce ventricular fibrillation (*9*). Inhibition of such heterogeneous myocardial cellular mechanisms or control of modulated sympathetic tone could be another possible explanation.

The present study used a gradual total occlusion of the proximal of LAD, as evidenced by the coronary angiography (Fig. 4), and thus caused an MI of approximately 27% of the total myocardium. The global LV ejection fraction in group B was significantly reduced (39% vs. 66% in controls), showing that LV systolic function was impaired in group B. Both histology and PET had concordant findings. The baseline MBF in the MI area was reduced and was not responding to adenosine administration. This finding is reasonable because the infarcted tissue should have reduced capillary density, and the resistive vessels do not respond to any vasodilating stimulation. The physical extent and size of the MI were reproducible among the individual animals. This feature is important when this animal model is applied to evaluate various new pharmaceuticals or various regenerative therapeutic trials.

The noninfarcted myocardium developed clear signs of remodeling, such as hypokinesis, hypertrophy, and the accumulation of fibrotic tissue in the remote myocardial wall, and significantly decreased PTI values, a marker of residual fractionation of water-perfusable tissue. The baseline MBF was preserved, but reactivity to the adenosine was blunted, even at a maximum dose of 600 μg/kg/min. This reduced reactivity could be related to the degeneration of small arteries, possibly caused by enlargement of myocytes and development of moderate denaturation necrosis and fibrosis.

This study demonstrated that physiologic status and physical extent of MI can be evaluated using the noninvasive technique of PET. The defect surface area identified with ^{18}F-FDG was identical to that identified with PTF, and both agreed well with the results of histology. Furthermore, microscopic degeneration can be characterized as reduced reactivity of quantitative myocardial perfusion to adenosine. The PET-derived PTI, which is known to indicate the absolute fraction of non–scar tissue within the area (*22*), was reduced not only in the infarcted anterior wall but also in the remote region by 10%. As demonstrated in recent studies (*31–34*), the reduced PTI in a control region is thought to be caused by the development of microscopic fibrosis.

In this study, left-atrial and LV pressure analyses have not been measured, because the aims of this study were to create a long-survival pig model of MI and global LV dysfunction with remodeling, characterize this model using PET, and compare these parameters with histology before making a complete model of CHF after MI in pigs. One limitation of this study was that, because of technical reasons in our laboratory at the initiation of this study, it was difficult to measure left-atrial and LV pressures.

CONCLUSION

Our pig model of postinfarction global LV dysfunction was characterized by a high survival rate and large MI, with clear signs of cardiac remodeling, as demonstrated by PET and histology. This animal model might contribute to investigations of MI and new therapies for cardiac remodeling in MI.

ACKNOWLEDGMENTS

REFERENCES

1. Saito I, Folsom AR, Aono H, Ozawa H, Ikebe T, Yamashita T. Comparison of fatal coronary heart disease occurrence based on population surveys in Japan and the USA. *Int J Epidemiol.* 2000;29:837–844.
2. Balady GJ, Jette D, Scheer J, Downing J. Changes in exercise capacity following cardiac rehabilitation in patients stratified according to age and gender: results of the Massachusetts Association of Cardiovascular and Pulmonary Rehabilitation Multicenter Database. *J Cardiopulm Rehabil.* 1996;16:38–46.
3. Krum H, Haas SJ, Eichhorn E, et al. Prognostic benefit of beta-blockers in patients not receiving ACE-inhibitors. *Eur Heart J.* 2005;26:2154–2158.
4. Anversa P, Leri A, Kajstura J. Cardiac regeneration. *J Am Coll Cardiol.* 2006;47:1769–1776.
5. Gheeraert PJ, Henriques JP, De Buyzere ML, De Pauw M, Taeymans Y, Zijlstra F. Preinfarction angina protects against out-of-hospital ventricular fibrillation in patients with acute occlusion of the left coronary artery. *J Am Coll Cardiol.* 2001;38:1369–1374.
6. Millard RW. Induction of functional coronary collaterals in the swine heart. *Basic Res Cardiol.* 1981;76:468–473.
7. Roth DM, Maruoka Y, Rogers J, White FC, Longhurst JC, Bloor CM. Development of coronary collateral circulation in left circumflex Ameroid-occluded swine myocardium. *Am J Physiol.* 1987;253:H1279–H1288.
8. Fallavollita JA, Riegel BJ, Suzuki G, Valeti U, Canty JM Jr. Mechanism of sudden cardiac death in pigs with viable chronically dysfunctional myocardium and ischemic cardiomyopathy. *Am J Physiol Heart Circ Physiol.* 2005;289:H2688–H2696.
9. Canty JM Jr, Suzuki G, Banas MD, Verheyen F, Borgers M, Fallavollita JA. Hibernating myocardium: chronically adapted to ischemia but vulnerable to sudden death. *Circ Res.* 2004;94:1142–1149.
10. Fallavollita JA, Canty JM Jr. Differential ^{18}F-2-deoxyglucose uptake in viable dysfunctional myocardium with normal resting perfusion: evidence for chronic stunning in pigs. *Circulation.* 1999;99:2798–2805.
11. Fallavollita JA, Canty JM Jr. Ischemic cardiomyopathy in pigs with two-vessel occlusion and viable, chronically dysfunctional myocardium. *Am J Physiol Heart Circ Physiol.* 2002;282:H1370–H1379.
12. Fallavollita JA, Logue M, Canty JM Jr. Stability of hibernating myocardium in pigs with a chronic left anterior descending coronary artery stenosis: absence of progressive fibrosis in the setting of stable reductions in flow, function and coronary flow reserve. *J Am Coll Cardiol.* 2001;37:1989–1995.
13. Shen YT, Vatner SF. Mechanism of impaired myocardial function during progressive coronary stenosis in conscious pigs: hibernation versus stunning? *Circ Res.* 1995;76:479–488.
14. Mills I, Fallon JT, Wrenn D, et al. Adaptive responses of coronary circulation and myocardium to chronic reduction in perfusion pressure and flow. *Am J Physiol.* 1994;266:H447–H457.
15. Roth DM, White FC, Nichols ML, Dobbs SL, Longhurst JC, Bloor CM. Effect of long-term exercise on regional myocardial function and coronary collateral development after gradual coronary artery occlusion in pigs. *Circulation.* 1990;82:1778–1789.
16. Shen YT, Lynch JJ, Shannon RP, Wiedmann RT. A novel heart failure model induced by sequential coronary artery occlusions and tachycardiac stress in awake pigs. *Am J Physiol.* 1999;277:H388–H398.
17. *Guide for the Care and Use of Laboratory Animals.* Washington, DC: National Academy Press; 1996.
18. O'Konski MS, White FC, Longhurst J, Roth D, Bloor CM. Ameroid constriction of the proximal left circumflex coronary artery in swine: a model of limited coronary collateral circulation. *Am J Cardiovasc Pathol.* 1987;1:69–77.
19. Iida H, Takahashi A, Tamura Y, Ono Y, Lammertsma AA. Myocardial blood flow: comparison of oxygen-15-water bolus injection, slow infusion and oxygen-15-carbon dioxide slow inhalation. *J Nucl Med.* 1995;36:78–85.
20. DeFronzo RA, Tobin JD, Andres R. Glucose clamp technique: a method for quantifying insulin secretion and resistance. *Am J Physiol.* 1979;237:E214–E223.
21. Knuuti MJ, Nuutila P, Ruotsalainen U, et al. Euglycemic hyperinsulinemic clamp and oral glucose load in stimulating myocardial glucose utilization during positron emission tomography. *J Nucl Med.* 1992;33:1255–1262.
22. Iida H, Tamura Y, Kitamura K, Bloomfield PM, Eberl S, Ono Y. Histochemical correlates of ^{15}O-water-perfusable tissue fraction in experimental canine studies of old myocardial infarction. *J Nucl Med.* 2000;41:1737–1745.
23. Iida H, Rhodes CG, de Silva R, et al. Myocardial tissue fraction: correction for partial volume effects and measure of tissue viability. *J Nucl Med.* 1991;32:2169–2175.
24. Iida H, Rhodes CG, de Silva R, et al. Use of the left ventricular time-activity curve as a noninvasive input function in dynamic oxygen-15-water positron emission tomography. *J Nucl Med.* 1992;33:1669–1677.
25. de Silva R, Yamamoto Y, Rhodes CG, et al. Preoperative prediction of the outcome of coronary revascularization using positron emission tomography. *Circulation.* 1992;86:1738–1742.
26. Yamamoto Y, de Silva R, Rhodes CG, et al. A new strategy for the assessment of viable myocardium and regional myocardial blood flow using ^{15}O-water and dynamic positron emission tomography. *Circulation.* 1992;86:167–178.
27. Moses MA, Addison PD, Neligan PC, et al. Inducing late phase of infarct protection in skeletal muscle by remote preconditioning: efficacy and mechanism. *Am J Physiol Regul Integr Comp Physiol.* 2005;289:R1609–R1617.
28. Kitakaze M, Node K, Minamino T, et al. Role of activation of protein kinase C in the infarct size-limiting effect of ischemic preconditioning through activation of ecto-5′-nucleotidase. *Circulation.* 1996;93:781–791.
29. Kharbanda RK, Mortensen UM, White PA, et al. Transient limb ischemia induces remote ischemic preconditioning in vivo. *Circulation.* 2002;106:2881–2883.
30. Chen PS, Chen LS, Cao JM, Sharifi B, Karagueuzian HS, Fishbein MC. Sympathetic nerve sprouting, electrical remodeling and the mechanisms of sudden cardiac death. *Cardiovasc Res.* 2001;50:409–416.
31. Knaapen P, Boellaard R, Gotte MJ, et al. Perfusable tissue index as a potential marker of fibrosis in patients with idiopathic dilated cardiomyopathy. *J Nucl Med.* 2004;45:1299–1304.
32. Knaapen P, Boellaard R, Gotte MJ, et al. The perfusable tissue index: a marker of myocardial viability. *J Nucl Cardiol.* 2003;10:684–691.
33. Knaapen P, Bondarenko O, Beek AM, et al. Impact of scar on water-perfusable tissue index in chronic ischemic heart disease: evaluation with PET and contrast-enhanced MRI. *Mol Imaging Biol.* 2006;8:245–251.
34. Knaapen P, van Dockum WG, Bondarenko O, et al. Delayed contrast enhancement and perfusable tissue index in hypertrophic cardiomyopathy: comparison between cardiac MRI and PET. *J Nucl Med.* 2005;46:923–929.

Quantification of regional myocardial oxygen metabolism in normal pigs using positron emission tomography with injectable ^{15}O-O_2

Takashi Temma · Hidehiro Iida · Takuya Hayashi · Noboru Teramoto · Youichiro Ohta · Nobuyuki Kudomi · Hiroshi Watabe · Hideo Saji · Yasuhiro Magata

Abstract

Purpose Although ^{15}O-O_2 gas inhalation can provide a reliable and accurate myocardial metabolic rate for oxygen by PET, the spillover from gas volume in the lung distorts the images. Recently, we developed an injectable method in which blood takes up ^{15}O-O_2 from an artificial lung, and this made it possible to estimate oxygen metabolism without the inhalation protocol. In the present study, we evaluated the effectiveness of the injectable ^{15}O-O_2 system in porcine hearts.

Methods PET scans were performed after bolus injection and continuous infusion of injectable ^{15}O-O_2 via a shunt between the femoral artery and the vein in normal pigs. The injection method was compared to the inhalation method. The oxygen extraction fraction (OEF) in the lateral walls of the heart was calculated by a compartmental model in view of the spillover and partial volume effect.

Results A significant decrease of lung radioactivity in PET images was observed compared to the continuous inhalation of ^{15}O-O_2 gas. Furthermore, the injectable ^{15}O-O_2 system provides a measurement of OEF in lateral walls of the heart that is similar to the continuous-inhalation method (0.71 ± 0.036 and 0.72 ± 0.020 for the bolus-injection and continuous-infusion methods, respectively).

Conclusion These results indicate that injectable ^{15}O-O_2 has the potential to evaluate myocardial oxygen metabolism.

Keywords Myocardial oxygen metabolism · PET · Pig · OEF · Injectable ^{15}O-O_2

Introduction

In the myocardium, fatty acid or glucose is used to produce energy by aerobic metabolism. Oxygen is one of the most important substrates closely related to the aerobic metabolism in the TCA cycle; thus, oxygen metabolism should be a direct reflection of myocardial metabolism of these substrates. Therefore, there has been considerable interest in the development of a method to quantify oxygen metabolism in the myocardium.

Recently, ^{11}C-acetate has been used for this purpose [1–5]. ^{11}C-acetate is taken up by the mitochondria and metabolically converted into acetyl-CoA. It then enters the TCA cycle and is transformed to ^{11}C-CO_2, which is cleared rapidly from the myocardium. Thus, the clearance pharmacokinetics reflects oxygen metabolism in the myocardium. However, the quantification of oxygen metabolism using ^{11}C-acetate is quite difficult because of various intermediary compounds.

The use of ^{15}O-O_2 gas inhalation and PET scanning can provide a quantitative myocardial metabolic rate for oxygen (MMRO$_2$) [6, 7]. The tracer kinetic model used is based on that originally proposed to describe the behavior of ^{15}O-O_2 in brain tissue [8, 9]. However, the direct translation of the

T. Temma · H. Saji
Department of Patho-Functional Bioanalysis,
Graduate School of Pharmaceutical Sciences, Kyoto University,
Kyoto, Japan

H. Iida · T. Hayashi · N. Teramoto · Y. Ohta · N. Kudomi ·
H. Watabe
Department of Investigative Radiology,
National Cardiovascular Center Research Institute,
Osaka, Japan

Y. Magata (✉)
Laboratory of Genome Bio-Photonics,
Photon Medical Research Center,
Hamamatsu University School of Medicine,
1-20-1 Handayama,
Hamamatsu 431-3192, Japan
e-mail: magata@hama-med.ac.jp

compartmental model for the brain to the heart is not permitted, because subtraction for spillover from gas volume in addition to that from the blood pool is needed. A previous study demonstrated that the gas volume can be accurately estimated from the transmission scan data; thus, this technique did not require additional emission scanning for estimating the quantitative gas volume images [6, 7]. However, gaseous radioactivity in the lung during the inhalation of ^{15}O-O$_2$ gas is too high in comparison to other regions. Subtraction for this contribution is straightforward and accurate using the transmission scan-derived gaseous volume images, but the lung radioactivity degraded image quality in the estimated MMRO$_2$ images.

As an alternative to gas inhalation, we recently developed a method to prepare an injectable form of ^{15}O-O$_2$. This was accomplished by exposing pre-collected blood to ^{15}O-O$_2$ gas using a small artificial lung system resulting in a maximum yield of 130 MBq/ml. We demonstrated that cerebral oxygen metabolism could be estimated in normal and ischemic rats using injectable ^{15}O-O$_2$ [10–12]. This technique has the potential of avoiding the inhalation protocol.

The aim of the present study was therefore to test the feasibility of using the injectable ^{15}O-O$_2$ oxygen system for estimating myocardial oxygen metabolism in pigs. The injection method was compared to the inhalation method to determine if the injection method resulted in a reduction of lung radioactivity, an improved image quality, a more accurate estimate of myocardial oxygen metabolism, and an improved signal-to-noise ratio.

Materials and methods

Theory

^{15}O-Oxygen was administered by IV injection or inhalation and was carried as ^{15}O-hemoglobin by blood to peripheral tissues including the myocardium, where it was converted to ^{15}O-water (^{15}O-H$_2$O$_{met}$) through aerobic metabolism. The increased distribution volume of ^{15}O-H$_2$O$_{met}$, represented by the exchangeable water space of tissue, causes delayed removal of radioactivity. This allows the definition of an appropriate model and equations to be derived for the calculation of a regional myocardial metabolic rate for oxygen (rMMRO$_2$) and regional oxygen extraction fraction (rOEF). Previous studies demonstrated that these calculations were similar to those used for estimating cerebral blood flow and oxygen metabolism and require the measurement of regional myocardial blood flow (rMBF) and a correction for spillover of activity from the vascular pools and the pulmonary alveoli [6, 7]. rMBF was measured by the ^{15}O-H$_2$O injection technique [13]. Activity in the vascular

pools of the heart chambers and the lung was evaluated with a conventional measurement of blood volume using ^{15}O-CO, and activity in the pulmonary alveoli was evaluated with an unconventional and indirect measurement of gas volume obtained from the transmission scan. Furthermore, the existence of recirculating ^{15}O-H$_2$O$_{met}$ in the blood freely accessible to the myocardium was taken into consideration.

The differential equation describing the myocardial kinetics after administration of ^{15}O-O$_2$ can be written as follows:

$$\frac{dC^{myo}(t)}{dt} = OEF \cdot f \cdot A_o(t) + f \cdot A_w(t) - \left(\frac{f}{p} + \lambda\right)C^{myo}(t) \quad (1)$$

where $C^{myo}(t)$ designates the true radioactivity concentration in the myocardium at time t, f is myocardial blood flow, $A_O(t)$ is the ^{15}O-O$_2$ radioactivity concentration in arterial blood, $A_w(t)$ is the ^{15}O-H$_2$O radioactivity concentration in arterial blood, p is the myocardium/blood partition coefficient of water, and λ is the physical decay constant of O-15.

Solving Eq. (1) in terms of $C^{myo}(t)$ gives:

$$C^{myo}(t) = OEF \cdot f \cdot A_o(t)*e^{-\left(\frac{f}{p}+\lambda\right)\cdot t} + f \cdot A_w(t)*e^{-\left(\frac{f}{p}+\lambda\right)\cdot t} \quad (2)$$

where the asterisk denotes the convolution integral. During steady-state conditions under the continuous administration of ^{15}O-O$_2$, the following relationship holds:

$$C^{myo} = \frac{OEF \cdot f \cdot A_o + f \cdot A_w}{\left(\frac{f}{p} + \lambda\right)} \quad (3)$$

In the actual PET studies, the spillover from vascular pools and pulmonary alveoli and the partial volume effect should be taken into consideration [14]. Then, the measured radioactivity concentration in the region of interest (ROI) in the myocardium ($R^{myo}(t)$) can be expressed as:

$$\begin{aligned} R^{myo}(t) &= \alpha \cdot C^{myo}(t) \\ &+ (V_B^{myo} \cdot A_t(t) - \alpha \cdot F_{Vein} \cdot OEF \cdot A_o(t) - \alpha \cdot F_{Vein} \cdot A_w(t)) \\ &+ V_G^{myo} \cdot C_{gas}(t) \end{aligned} \quad (4)$$

where α denotes the myocardial tissue fraction, V_B^{myo} is the myocardial blood volume, $A_t(t)$ is the total O-15 radioactivity concentration in arterial blood, F_{Vein} is the microscopic venous blood volume, V_G^{myo} is the gas volume in the myocardial ROI and $C_{gas}(t)$ is the O-15 radioactivity concentration in V_G^{myo}.

With the bolus injection or infusion methods using an artificial lung system, the radioactivity in the pulmonary alveoli is expected to be negligible in comparison with the inhalation method. Thus, Eq. (4) can be converted to:

$$R^{myo}(t) = \alpha \cdot C^{myo}(t)$$
$$+ (V_B^{myo} \cdot A_t(t) - \alpha \cdot F_{Vein} \cdot OEF \cdot A_o(t) - \alpha \cdot F_{Vein} \cdot A_w(t)) \tag{5}$$

Subjects

In this study, four healthy miniature pigs (22–30 kg) were used. The pigs were anesthetized by IM injection of ketamine and xylazine followed by continuous infusion of propofol (5 mg/kg/h). The animals were then placed in the supine position on the bed of the PET scanner. All experimental procedures were approved by the local animal welfare committee.

Injectable ^{15}O-O$_2$ preparation

In the "injection" study, injectable ^{15}O-O$_2$ was used. Injectable ^{15}O-O$_2$ was prepared as described previously [10–12]. In brief, part of an infusion line kit (Terumo Corporation, Tokyo, Japan) and an artificial lung 18 cm in length (Senko Medical Instrument Mfg Co. Ltd., Tokyo, Japan) were connected using silicone tubing to make a closed system. Then, venous blood collected from a pig, which was used in the following PET studies, was added to the system and circulated (100 ml/min) by a peristaltic pump, followed by introduction of ^{15}O-O$_2$ gas (~7,000 MBq/min/433 ml) into the artificial lung for 15 min to prepare injectable ^{15}O-O$_2$ (5.6–60.7 MBq/ml).

In the "continuous infusion" study, the left femoral artery and right femoral vein were both cannulated. The two cannulas from the artery and the vein were connected to the opposite sides of an artificial lung to create a femoral shunt. The blood flow in the shunt was aided by a peristaltic pump (30–50 ml/min). ^{15}O-O$_2$ gas (~7,000 MBq/min/433 ml) was continuously introduced into the artificial lung.

PET protocol (Fig. 1)

The PET scanner was an ECAT EXACT HR (CTI/Siemens) [15], which has an imaging field of view (FOV) of 55 cm in diameter and 15 cm in axial length. The spatial resolution of the scanner is 5.8 mm in full width at half maximum at the center of the FOV.

After obtaining a 20-min transmission scan for attenuation correction and gas volume estimation, the blood pool image was obtained with a 4-min PET scan after the pigs inhaled 2.7 GBq ^{15}O-CO for 30 s. Arterial blood samples were taken every minute during the ^{15}O-CO scanning, and
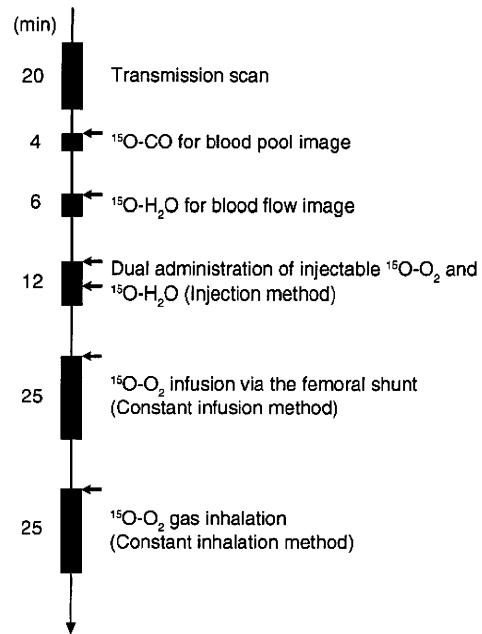
Fig. 1 Outline of the PET imaging study. The interval between scans was more than 15 min to allow for physical decay of O-15 radioactivity to background levels

the radioactivity concentration in the whole blood was measured with a NaI well-type scintillation counter calibrated against the PET scanner. Subsequently, ^{15}O-water was injected into the right femoral vein for 30 s at an infusion rate of 10 ml/min (injected radioactivity was about 1.11 GBq). Immediately after injection of ^{15}O-water, 26 dynamic frames (12×5 s, 8×15 s and 6×30 s) of PET data were acquired for 6 min.

Furthermore, two PET scans were successively performed after the IV injection of ^{15}O-O$_2$ (5.6–60.7 MBq/ml) for 30 s at an injection rate of 20–80 ml/min for the "injection" study, and by the continuous ^{15}O-O$_2$ gas infusion through the artificial lung in the femoral shunt for the "continuous infusion" study. In the "injection" study, 52 dynamic frames (12×5 s, 8×15 s, 6×30 s, 12×5 s, 8×15 s and 6×30 s) of PET data were acquired for 12 min, and 1.11 GBq of ^{15}O-water was injected IV for 30 s at 10 ml/min starting at 6 min after the administration of IV ^{15}O-O$_2$ according to the dual administration protocol we developed previously [16]. In the "continuous infusion" study, 26 dynamic frames (10×30 s, 5×60 s, 1×600 s and 10×30 s) were acquired for 25 min, and the 600-s frame was used for steady-state analysis.

Another PET scan was performed by ^{15}O-O$_2$ gas inhalation in one of the four pigs in the same protocol as the "continuous infusion" study. This was the "continuous inhalation" study. The interval between scans was more

than 15 min to allow for physical decay of O-15 radioactivity to background levels. All acquisitions were obtained in the two-dimensional mode (septa extended).

Data analysis

A filtered back-projection algorithm with a 6-mm Gaussian filter was used for image reconstruction. The reconstructed images had a matrix size of 128 × 128 × 47 and a voxel size of 1.84 × 1.84 × 3.38 mm, and all image data sets were resliced into short-axis images across the left ventricle [13].

Myocardial blood flow

rMBF was calculated from the injection of ^{15}O-H_2O by fitting the myocardial and arterial time-activity curve data to a single-tissue-compartment model that implemented corrections for partial-volume effects by introducing the tissue fraction. In addition, the model was corrected for spillover from the left ventricular (LV) chamber into the myocardial ROI by introducing the arterial blood volume [13]. In these experiments, the time-activity curves generated from large ROIs placed in the LV chamber were used as the input function.

Regional oxygen extraction fraction

In the "injection" study, rOEF was calculated according to Eqs. (2) and (5). In these formulations, F_{vein} was assumed to be 0.10 ml/g tissue and p was fixed at 0.90 ml/g. The blood volume image obtained from the ^{15}O-CO scan was used for the determination of V_B^{myo}. The value of $A_t(t)$ was obtained from the LV radioactivity concentration measured from the PET data set with small LV ROIs to minimize spillover from the myocardium. The calculation for the estimation of recirculating ^{15}O-H_2O was performed as previously described [16]. For the "continuous infusion" and "continuous inhalation" studies, in which a 600-s frame was regarded as steady-state, Eqs. (3) and (5) or Eqs. (3) and (4) were used for calculating rOEF, respectively.

Results

Table 1 summarizes the conditions of animals during the PET studies. The parameters were all within the physiologic range.
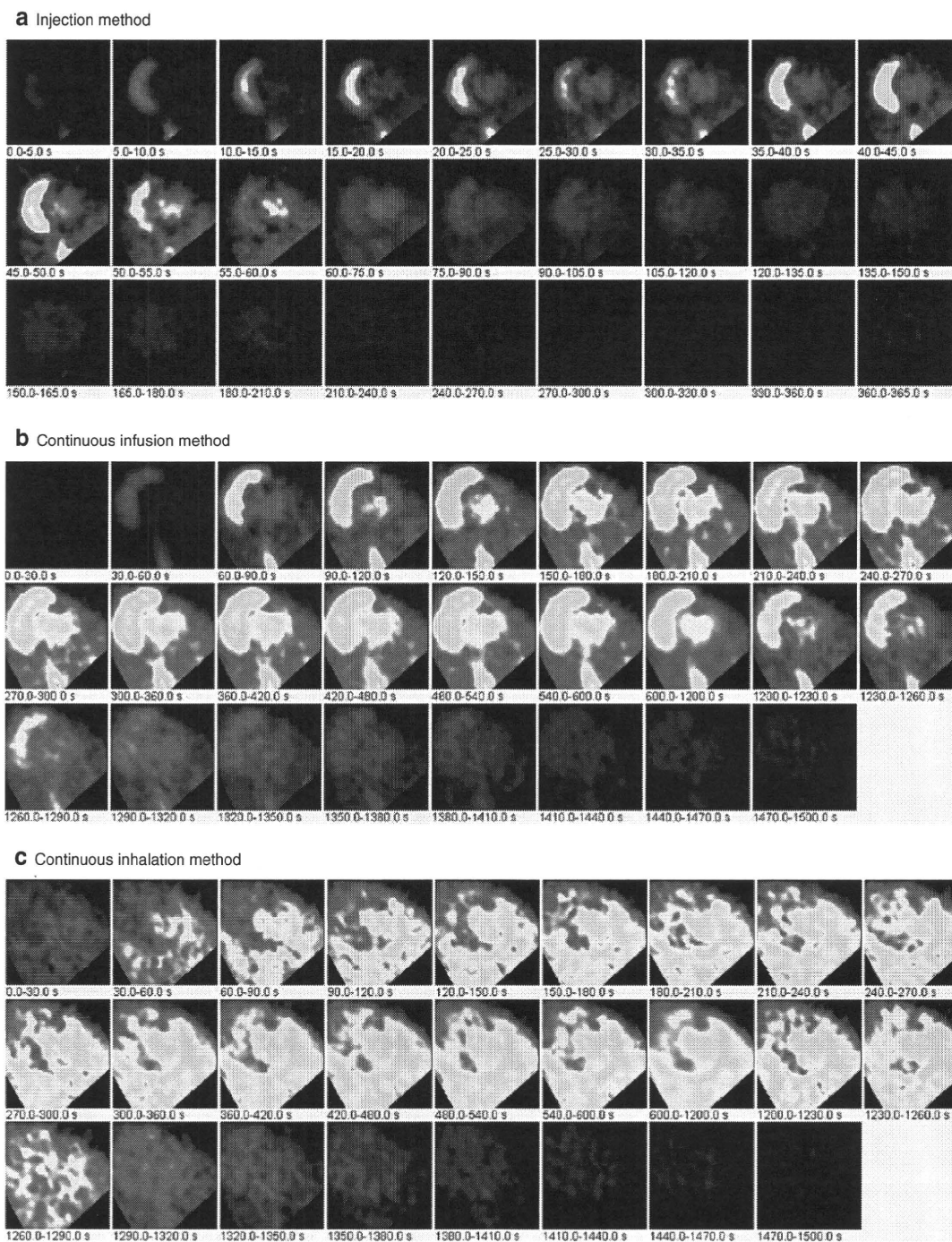
Figure 2 demonstrates the dynamic images obtained in the "injection", "continuous infusion", and "continuous inhalation" studies. With the injection and continuous-infusion methods, the right ventricle on the left side and the vena cava on the lower side were well delineated, whereas the left ventricle was moderately shown on the right side. The 16th frame (600~1,200 s after the initiation), which was used for steady-state analysis with the continuous-infusion method, was visibly distinct compared with all of the frames obtained with the injection method. However, with the continuous-inhalation method, neither ventricle could be depicted because of high radioactivity in the lung on the right and lower-side images.

The radioactivity in the blood pool obtained by ^{15}O-CO PET (Fig. 3g) and the gaseous volume estimated by inverse transmission data (Fig. 3h) were subtracted from the raw PET images (16th frame) with the continuous-inhalation and continuous-infusion methods, respectively (Fig. 3c and f). Both methods clearly delineated the myocardium after subtraction in comparison to the blood flow image (Fig. 3i). However, the continuous-inhalation method showed salient radioactivity on the lateral wall (Fig. 3c), whereas the continuous-infusion method showed only modest radioactivity in the myocardium (Fig. 3f). It is also notable that there was considerable radioactivity in the right ventricle with the continuous-infusion method even after the subtraction (Fig. 3f).

To further examine the differences between the continuous-infusion and continuous-inhalation methods, time-radioactivity curves during the PET scans were taken from four ROIs: the left ventricle (LV), right ventricle (RV), myocardium (Myo), and lung (Fig. 4). At the steady-state frame (600~1,200 s), the continuous-infusion method showed higher radioactivity in the RV and LV than in the myocardium (Fig. 4a), whereas the radioactivity of these regions was similar with the continuous-inhalation method (Fig. 4b). The radioactivity in LV was about two-thirds of that in RV in Fig. 4a, indicating that measurable radioactivity was excreted through the lung even after the femoral administration of ^{15}O-O_2. The lung excretion was also observed on the blood-subtracted image (Fig. 3e). Actually, there was significant radioactivity in the lung (Fig. 4a), although that was the lowest among the four ROIs. In contrast, the radioactivity in the myocardium was the lowest among the four ROIs with the continuous-inhalation method

| Table 1 Physiological parameters of pigs during the PET studies	pH	pCO$_2$ (mmHg)	pO$_2$ (mmHg)	tHb (g/dl)	O$_2$Sat (%)	HR (bpm)	BP (mmHg)	
							Diastolic	Systolic
Average	7.46	40.3	125.8	12.8	97.7	85	97.8	125.2
SD	0.032	2.51	16.69	1.30	1.83	19.5	10.4	19.3

Fig. 2 PET images obtained in (**a**) the injection method, (**b**) the continuous-infusion method with injectable ^{15}O-O_2, and (**c**) the continuous-inhalation method with ^{15}O-O_2 gas

(Fig. 4b). The heart-to-lung radioactivity ratios were calculated from Fig. 4 for the quantitative estimation of image quality; the continuous-infusion method provided a ratio of 1.38±0.24, whereas the ratio was less than one with the continuous-inhalation method.

Table 2 shows the quantitative OEF values in the lateral wall obtained by the injection, continuous-infusion, and continuous-inhalation methods. These OEF values were consistent among the three methods.

Figure 5 represents the noise equivalent counts (NEC) standardized by the total counts detected by the PET scanner. Although the injection method tended to show rather high values, there was no significant difference between the values obtained by the injection and
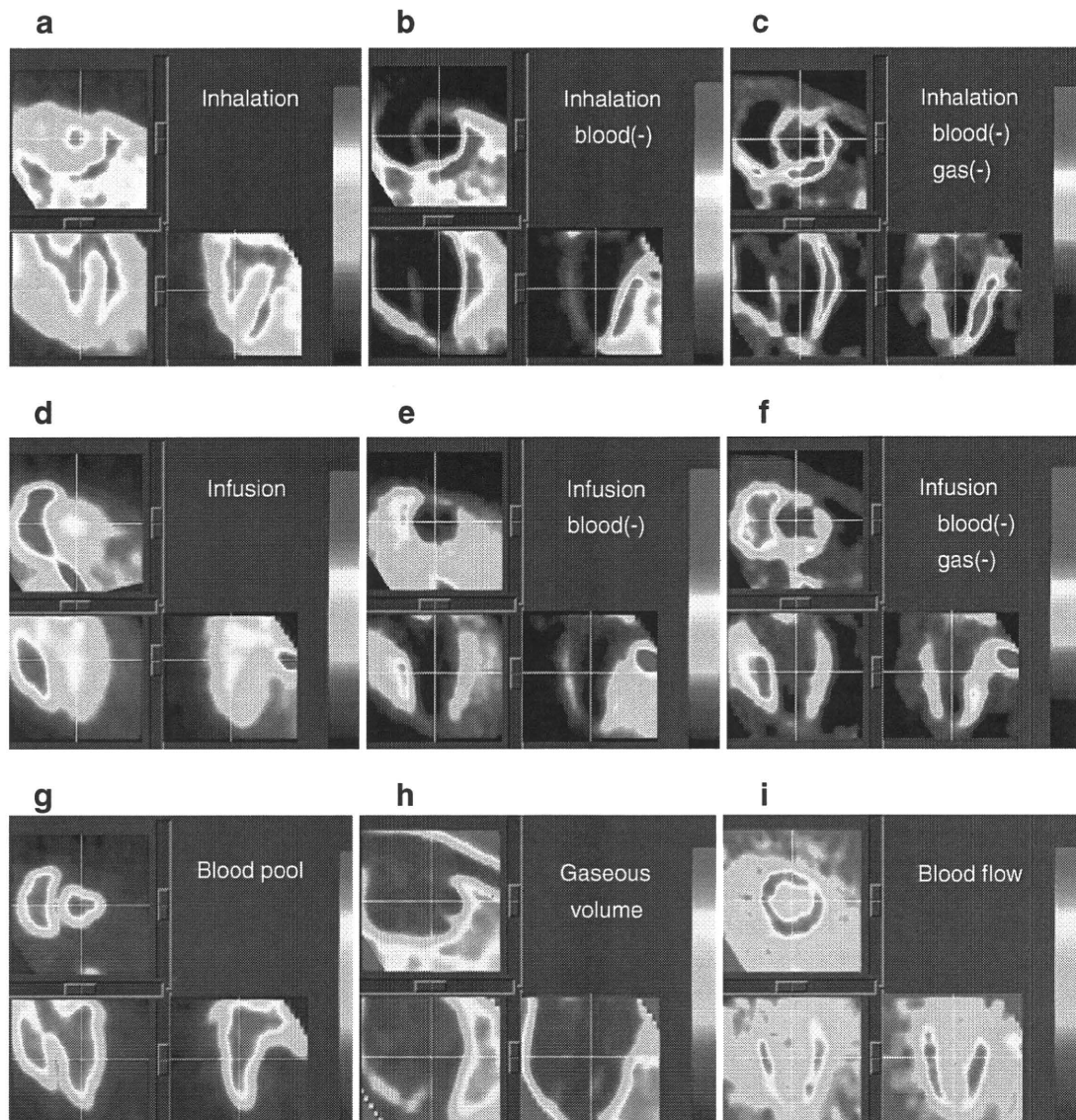
Fig. 3 PET images obtained in the study are shown. The 16th frame (steady-state frames) of the continuous-inhalation method and the continuous-infusion method are shown in (**a**) and (**d**), respectively. The 'blood-subtracted' images shown in (**b**) and (**e**) were created by subtraction of the blood-pool image by ^{15}O-CO (**g**) from (**a**) and (**d**). The 'blood- and gas-subtracted' images shown in (**c**) and (**f**) were created by the successive subtraction of the gaseous image (**h**) from (**b**) and (**e**). The myocardial blood flow image is also shown in (**i**)

continuous-infusion methods as determined by a Mann Whitney U-test.

Discussion

In previous studies, we showed the usefulness of the injectable ^{15}O-O$_2$ system for estimating cerebral oxygen metabolism in small animals such as rats under normal or ischemic conditions [10–12]. Injectable ^{15}O-O$_2$ replaced the inhalation protocol and radioactive ^{15}O-O$_2$ was administered via the tail vein. Thus, injectable ^{15}O-O$_2$ could abolish the artifact from the high radioactivity in the inhalation tube that distorts the PET images, especially in small animals. We considered that the concept could also be utilized in the hearts of large animals. Therefore, in the present study, we tested the feasibility of an injectable ^{15}O-O$_2$ system for estimating myocardial oxygen metabolism in normal pigs. In addition, since a shunt between the femoral artery and vein can be created in pigs but not in small animals, continuous infusion via the femoral shunt was also performed to achieve a constant and reliable delivery of radioactivity to the heart.

Dynamic PET scans showed a large difference in the radioactivity distribution among the three methods. Since the labeling efficiency to prepare injectable ^{15}O-O$_2$ was

a Continuous infusion

b Continuous inhalation
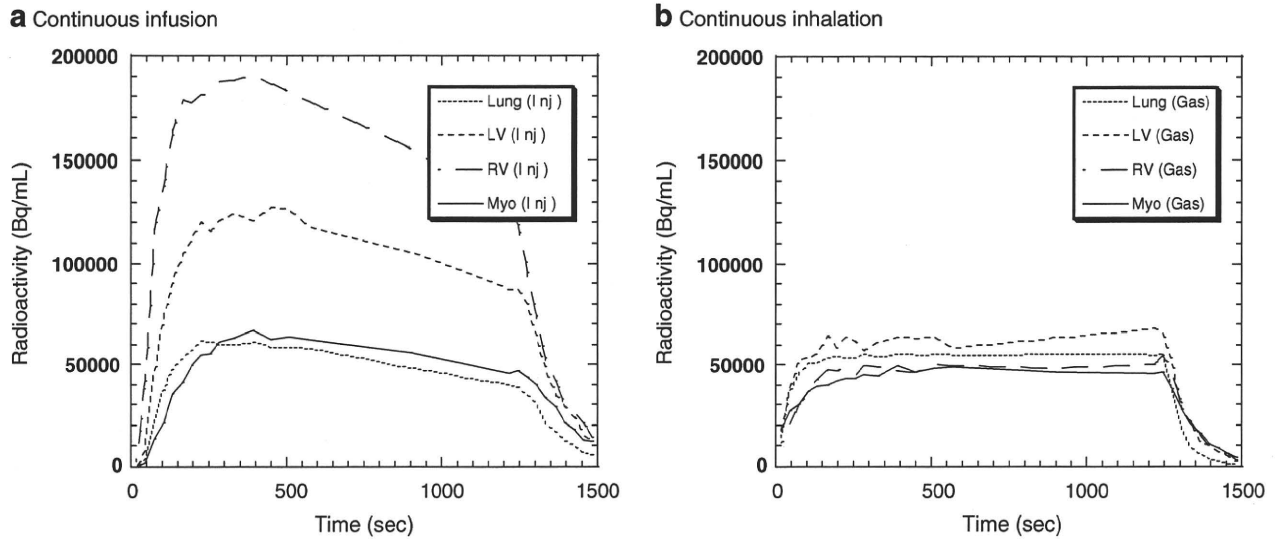
Fig. 4 Time-activity curves from the left ventricle (*LV*), the right ventricle (*RV*), the myocardium (lateral wall, Myo) and a lung region with the continuous-infusion method (**a**) and the continuous-inhalation method (**b**). The supply of radioactivity was started at time 0 s and stopped at 1,200 s. The 16th frame for the steady-state analysis was 600–1,200 s

lower with pig blood (ca. 61 MBq/ml at most) than with the blood of rats and humans (130 MBq/ml), the injection method provided rather obscure images. With the injection and continuous-infusion methods, the radioactivity in the lung was dramatically reduced in comparison to the continuous-inhalation method, since the heart-to-lung ratio with the continuous-infusion method was about 40% higher than with the continuous-inhalation method. This finding suggested that the two methods that inject radioactivity via a vein are more useful for analyzing myocardial oxygen metabolism in pigs than the continuous-inhalation method. However, a distinct difference between radioactivity of the right and left ventricles was observed in the images and time-radioactivity curves after venous administration of ^{15}O-O$_2$, indicating a certain degree of excretion of the radioactivity by the lung. Therefore, the spillover from the pulmonary alveoli to the myocardium could not be omitted in the two methods with venous administration, and Eq. (4)

was used for the OEF analysis, although the radioactivity in the lung was lower than that in the myocardium.

On the other hand, with the continuous-inhalation method, the radioactivity of the lung was in between the radioactivity in the RV and LV. This is curious because O-15 radioactivity was supplied from the inhalation tube and transferred from the lung to blood so that the radioactivity in the lung should have been the highest among the four ROIs. This may have been caused, in part, by inhomogeneous distribution of the radioactivity in the lung due to its structure in comparison with the myocardium and ventricles, and/or by artifacts from the lung to other

Table 2 OEF estimated by the three methods using injectable ^{15}O-O$_2$ or ^{15}O-O$_2$ gas

	OEF		
	Injection	Infusion	Inhalation
Pig. 1	0.70	0.72	
Pig. 2	0.67	0.72	
Pig. 3	0.71	0.74	
Pig. 4	0.76	0.69	0.72
Average	0.71	0.72	0.72
SD	0.036	0.020	
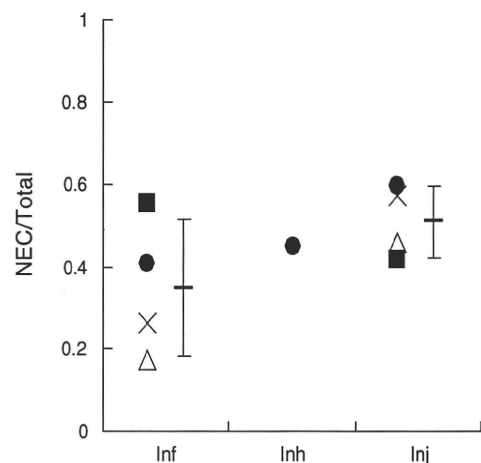
Fig. 5 The ratio of noise equivalent counts (*NEC*) to total counts in the total field of view of the PET scanner obtained with the continuous-infusion method (*Inf*), the continuous-inhalation method (*Inh*) and the injection method (*Inj*)

tissues. In any case, it is notable that the radioactivity in the myocardium was the lowest with the continuous-inhalation method, leading to difficulty in analyzing myocardial oxygen metabolism.

The OEF values in lateral walls were calculated to compare the ability of the three methods to determine myocardial oxygen metabolism by using the blood flow derived from the dual-administration protocol with the injection method and the single-administration protocol with the two continuous methods. There was no difference in the blood flow between the two protocols. Consequently, the three methods provided the same OEF value of about 0.7 and this is a physiological value in normal pigs, as was previously demonstrated [17, 18]. We have demonstrated the potential of the injectable ^{15}O-O$_2$ system for the estimation of physiological cerebral oxygen metabolism in rats and monkeys during early and late ischemia, hypertension, and ischemia plus hypertension [10–12, 19]. Therefore, we believe that the injection and continuous-infusion methods provide a physiological OEF in the myocardium. Nevertheless, we recognize the necessity to evaluate the reliability and usefulness of the injectable ^{15}O-O$_2$ method in myocardial applications. Further studies using pathophysiological animal models are required in the future, such as myocardial ischemia, hypoxia, and heart failure. On the other hand, since MMRO$_2$ is basically regarded as the product of MBF and OEF, the results indicated that these three methods were equivalent in their ability to quantify MMRO$_2$ in normal pigs, at least in the lateral wall. Although the images after the subtraction of spillovers from blood and gas showed different contrast between the continuous-infusion and continuous-inhalation methods, the ability of these two methods to measure OEF and MMRO$_2$ in the lateral walls was equivalent.

We did not evaluate myocardial oxygen metabolism in other heart regions since the radioactivity in the right ventricle could not be removed due to a significant difference of radioactivity between the ventricles with the continuous-infusion method. The injection method might be able to evaluate oxygen metabolism in other regions besides the lateral wall, although this was not evaluated in this study due to the low radioactivity of injectable ^{15}O-O$_2$ as described above. In the injection method, O-15 radioactivity was delivered from the femoral vein to RV, the lung, LV, and finally the myocardium. Thus, when the LV and myocardial activity reach a maximum, the RV activity is expected to be low. The later frames of the dynamic PET images with the injection method might avoid the high RV activity and delineate the myocardium and LV more clearly. With accurate anatomical information by gated PET/CT, the injection method will provide oxygen metabolism in other heart regions. In addition, the injection method has a benefit in that it is noninvasive and shortens the acquisition time in comparison with the continuous-infusion method. Future studies are needed to determine whether the injectable ^{15}O-O$_2$ system can be used in other heart regions.

With the injection method, the ratio of noise equivalent counts (NEC) to total counts tended to be the higher, probably because of the absence of high radioactivity adjacent to the PET scanner. Nevertheless, the continuous-infusion method did not show this tendency. This may be because tubes for the input to the artificial lung were positioned at the femoral shunt and the output to the drain of O-15 gas was positioned alongside the PET scanner, resulting in an increase of random counts during the study. Also, it is notable that the value with the continuous-inhalation method was not small, which suggests that the inhalation protocol itself did not worsen the results, but rather the high radioactivity in the lung might affect the analysis. In any case, if more care is given to shielding of the radioactivity in tubes and/or for arrangement of instruments in the PET room, a higher value of NEC/total counts will be obtained with the injectable ^{15}O-O$_2$ system.

The declining slope delineated in the time-activity curves with the continuous-infusion method requires some explanation. Since the flow rate of O-15 gas supply to the artificial lung positioned at the femoral shunt was maintained constant during the PET scan, it is possible that a decrease of labeling efficiency of the artificial lung occurred due to the deposition of any components of blood. The blood of rats or humans was negligibly deposited in the artificial lung during circulation at the same rate for at least 30 min in our other experiments, so that this problem may be specific for pigs. It is unclear which component in pig blood was exactly involved in the deposition and three of four pigs did not show a declining slope of the time-activity curve.

In practice, in routine studies on myocardial oxygen metabolism using large animals such as pigs, the continuous-inhalation method with ^{15}O-O$_2$ gas may be easier to perform for the following reasons: (1) the intubation tube used for gas anesthesia prior to the PET scan can also be used for ^{15}O-O$_2$ gas inhalation; (2) catheterization of the femoral artery and vein to create the femoral shunt for the continuous-infusion method may be troublesome; and (3) the injection of ^{15}O-O$_2$ requires an artificial lung, preparation time, and blood taken from the same animal prior to the PET scan. However, the injection of ^{15}O-O$_2$ has a substantial advantage over the continuous-inhalation method in that there is reduced radioactivity in the lung and clearer images of the heart are obtained. Therefore, the method for estimating myocardial oxygen metabolism should be selected depending on the objectives of the study and the surgical procedures. Furthermore, since radioactivity administered into the femoral vein is partially excreted into expired air, the injectable ^{15}O-O$_2$ system might be used for evaluating pulmonary function in the future.

Conclusion

In this study, we tested the feasibility of using an injectable ^{15}O-O_2 system to estimate myocardial oxygen metabolism in pigs. Both the bolus-injection and continuous-infusion methods reduced the radioactivity in the lung and provided similar OEF values in the lateral walls of the heart. These findings indicate that the injectable ^{15}O-O_2 system has the potential to evaluate myocardial oxygen metabolism.

References

1. Ohtake T. The review of myocardial positron emission computed tomography and positron imaging by gamma camera. Kaku Igaku. 1998;35:179–87.
2. Klein LJ, Visser FC, Knaapen P, Peters JH, Teule GJ, Visser CA, et al. Carbon-11 acetate as a tracer of myocardial oxygen consumption. Eur J Nucl Med. 2001;28:651–68.
3. Schelbert HR. PET contributions to understanding normal and abnormal cardiac perfusion and metabolism. Ann Biomed Eng. 2000;28:922–9.
4. Visser FC. Imaging of cardiac metabolism using radiolabelled glucose, fatty acids and acetate. Coron Artery Dis. 2001;12(Suppl 1):S12–8.
5. Hata T, Nohara R, Fujita M, Hosokawa R, Lee L, Kudo T, et al. Noninvasive assessment of myocardial viability by positron emission tomography with ^{11}C acetate in patients with old myocardial infarction. Usefulness of low-dose dobutamine infusion. Circulation. 1996;94:1834–41.
6. Yamamoto Y, de Silva R, Rhodes CG, Iida H, Lammertsma AA, Jones T, et al. Noninvasive quantification of regional myocardial metabolic rate of oxygen by $^{15}O_2$ inhalation and positron emission tomography. Experimental validation. Circulation. 1996;94:808–16.
7. Iida H, Rhodes CG, Araujo LI, Yamamoto Y, de Silva R, Maseri A, et al. Noninvasive quantification of regional myocardial metabolic rate for oxygen by use of $^{15}O_2$ inhalation and positron emission tomography. Theory, error analysis, and application in humans. Circulation. 1996;94:792–807.
8. Shidahara M, Watabe H, Kim KM, Oka H, Sago M, Hayashi T, et al. Evaluation of a commercial PET tomograph-based system for the quantitative assessment of rCBF, rOEF and rCMRO$_2$ by using sequential administration of ^{15}O-labeled compounds. Ann Nucl Med. 2002;16:317–27.
9. Mintun MA, Raichle ME, Martin WR, Herscovitch P. Brain oxygen utilization measured with O-15 radiotracers and positron emission tomography. J Nucl Med. 1984;25:177–87.
10. Magata Y, Temma T, Iida H, Ogawa M, Mukai T, Iida Y, et al. Development of injectable O-15 oxygen and estimation of rat OEF. J Cereb Blood Flow Metab. 2003;23:671–6.
11. Temma T, Magata Y, Kuge Y, Shimonaka S, Sano K, Katada Y, et al. Estimation of oxygen metabolism in a rat model of permanent ischemia using positron emission tomography with injectable ^{15}O-O_2. J Cereb Blood Flow Metab. 2006;26:1577–83.
12. Temma T, Kuge Y, Sano K, Kamihashi J, Obokata N, Kawashima H, et al. PET O-15 cerebral blood flow and metabolism after acute stroke in spontaneously hypertensive rats. Brain Res. 2008;1212:18–24.
13. Watabe H, Jino H, Kawachi N, Teramoto N, Hayashi T, Ohta Y, et al. Parametric imaging of myocardial blood flow with ^{15}O-water and PET using the basis function method. J Nucl Med. 2005;46:1219–24.
14. Iida H, Rhodes CG, de Silva R, Yamamoto Y, Araujo LI, Maseri A, et al. Myocardial tissue fraction–correction for partial volume effects and measure of tissue viability. J Nucl Med. 1991;32:2169–75.
15. Wienhard K, Dahlbom M, Eriksson L, Michel C, Bruckbauer T, Pietrzyk U, et al. The ECAT EXACT HR: performance of a new high resolution positron scanner. J Comput Assist Tomogr. 1994;18:110–8.
16. Kudomi N, Hayashi T, Teramoto N, Watabe H, Kawachi N, Ohta Y, et al. Rapid quantitative measurement of CMRO$_2$ and CBF by dual administration of ^{15}O-labeled oxygen and water during a single PET scan-a validation study and error analysis in anesthetized monkeys. J Cereb Blood Flow Metab. 2005;25:1209–24.
17. Alders DJ, Groeneveld AB, de Kanter FJ, van Beek JH. Myocardial O$_2$ consumption in porcine left ventricle is heterogeneously distributed in parallel to heterogeneous O$_2$ delivery. Am J Physiol Heart Circ Physiol. 2004;287:H1353–61.
18. Van Woerkens EC, Trouwborst A, Duncker DJ, Koning MM, Boomsma F, Verdouw PD. Catecholamines and regional hemodynamics during isovolemic hemodilution in anesthetized pigs. J Appl Physiol. 1992;72:760–9.
19. Temma T, Magata Y, Iida H, Hayashi T, Ogawa M, Mukai T, et al. Development of injectable O-15 oxygen and its application for estimation of OEF. International Congress Series, Quantitation in Biomedical Imaging with PET and MRI Proceedings of the International Workshop on Quantitation in Biomedical Imaging with PET and MRI. 2004;1265:262–65.

Slowly progressive neuronal death associated with postischemic hyperperfusion in cortical laminar necrosis after high-flow bypass for a carotid intracavernous aneurysm

Case report

Koji Iihara, M.D., Ph.D., Masakazu Okawa, M.D., Tomohito Hishikawa, M.D., Ph.D., Naoaki Yamada, M.D., Ph.D., Kazuhito Fukushima, M.D., Ph.D., Hidehiro Iida, Ph.D., and Susumu Miyamoto, M.D., Ph.D.

Departments of Neurosurgery and Radiology, National Cardiovascular Center, Osaka, Japan

The authors report a rare case of slowly progressive neuronal death associated with postischemic hyperperfusion in cortical laminar necrosis after radial artery/external carotid artery–middle cerebral artery bypass graft surgery for an intracavernous carotid artery aneurysm. Under barbiturate protection, a 69-year-old man underwent high-flow bypass surgery combined with carotid artery sacrifice for a symptomatic intracavernous aneurysm. The patient became restless postoperatively, and this restlessness peaked on postoperative Day (POD) 7. Diffusion-weighted and FLAIR MR images obtained on PODs 1 and 7 revealed subtle cortical hyperintensity in the temporal cortex subjected to temporary occlusion. On POD 13, ^{123}I-iomazenil (^{123}I-IMZ) SPECT clearly showed increased distribution on the early image and mildly decreased binding on the delayed image with count ratios of the affected–unaffected corresponding regions of interest of 1.23 and 0.84, respectively, suggesting postischemic hyperperfusion. This was consistent with the finding on ^{123}I-iodoamphetamine SPECT. Of note, neuronal density in the affected cortex on the delayed ^{123}I-IMZ image further decreased to the affected/unaffected ratio of 0.44 on POD 55 during the subacute stage when characteristic cortical hyperintensity on T1-weighted MR imaging, typical of cortical laminar necrosis, was emerging. The affected cortex showed marked atrophy 8 months after the operation despite complete neurological recovery. This report illustrates, for the first time, dynamic neuroradiological correlations between slowly progressive neuronal death shown by ^{123}I-IMZ SPECT and cortical laminar necrosis on MR imaging in human stroke. (*DOI: 10.3171/2009.9.JNS09345*)

Key Words • laminar necrosis • iomazenil • bypass •
delayed neuronal death • magnetic resonance imaging

ORTICAL laminar necrosis is a permanent brain injury radiologically characterized by T1-weighted MR imaging–documented high-intensity cortical lesions that follow the gyral anatomy of the cerebral cortex.[7,17,19] It has been associated with hypoxia, metabolic disturbances, drugs, infections, status epilepticus, and ischemic stroke.[7,19] The neuropathological correlations, however, between neuronal loss and an emerging cortical T1 hyperintensity signal in human stroke remain unknown. Intracavernous CA aneurysms are usually treated by trapping with/without EC-IC bypass based on presumed tolerance to CA sacrifice.[6,9] Flumazenil and iomazenil are markers of central benzodiazepine receptors, part of the GABAergic complex,[2] and are ideal markers

of periinfarct tissue and incomplete brain infarcts.[16] This is the first report illustrating slowly progressive neuronal death, shown by ^{123}I-IMZ, during emerging cortical laminar necrosis on MR imaging after temporary occlusion at high-flow bypass for an intracavernous CA aneurysm.

Case Report

History and Examination. This 69-year-old man developed double vision and ptosis due to left oculomotor palsy. Angiograms obtained at the previous hospital showed bilateral large intracavernous CA aneurysms (Fig. 1A). After balloon test occlusion showing intolerance on temporary occlusion of the left CA, the patient was referred to our institution.

Operation. The patient's left large CA aneurysm was trapped by RA/ECA-MCA bypass grafting without causing any neurological deficit. Temporary occlusion of the inferior trunk of M_2 was performed for 52 minutes under thiopental brain protection. Postoperative MR dif-

fusion weighted imaging demonstrated no abnormality. Two months later, the patient presented with contralateral oculomotor palsy due to progressive growth of the contralateral aneurysm. He underwent virtually the same operation, except with a shorter duration of temporary occlusion (47 minutes) and except for the observation that back flow from the distal M_2 was slower and dark when the distal clip was first declamped after anastomosis, suggesting that the territory of the recipient artery had been subjected to ischemic insult due to insufficient collateral flow.

Postoperative Course. The patient awoke from anesthesia relatively soon without apparent neurological deficit. Diffusion weighted and FLAIR imaging on POD 1 showed slight cortical hyperintensity in the right temporal region (Fig. 1C and D). Angiograms obtained on POD 5 showed no opacification of the aneurysm and good bypass patency, but the patient gradually became restless. Diffusion weighted and FLAIR imaging repeated on POD 7 revealed similar findings (Fig. 1E and F). Because the signal change on diffusion weighted imaging, however, remained subtle, the cause of such MR imaging abnormality remained uncertain. Subtle Gd enhancement was noted in the temporal cortex. On POD 18, ^{123}I-IMZ SPECT showed increased distribution on the early image (15 minutes) and decreased binding on the delayed image (3 hours) in the temporal region corresponding to the hyperintensity area on diffusion weighted and FLAIR images (Fig. 2). Because early and delayed images of ^{123}I-IMZ SPECT represent the cerebral perfusion state and neuronal viability, respectively, these results clearly indicated that ischemic neuronal loss and postischemic hyperperfusion occurred as a result of ischemic insult by temporary occlusion during bypass surgery.

Chronological count ratio changes of the affected to the unaffected corresponding regions of interest on ^{123}I-IMZ and ^{123}I-IMP SPECT scans are shown in Fig. 3. In the temporal region subjected to temporary clipping, the affected/unaffected ratio on ^{123}I-IMZ scans decreased during the subacute period between PODs 18 (ratio 0.84) and 55 (ratio 0.44), and then it leveled off later (ratio 0.43 on POD 239), whereas it remained relatively constant in other regions. We did not obtain ^{123}I-IMZ SPECT scans before the operation. On ^{123}I-IMP SPECT, the affected/unaffected ratio transiently increased during PODs 13 (ratio 1.21) and 26 (ratio 1.23), and it progressively decreased on PODs 53 (ratio 0.84) and 236 (ratio 0.67) in the temporal region, although virtually no changes were noted in other areas.

Correlation of SPECT and MR Imaging Findings. Serial FLAIR images showed cortical hyperintensity, which appeared on POD 1, peaked during PODs 7 and 13, almost returned to normal on POD 56, and demonstrated atrophy in the right temporal lobe on POD 237 (Fig. 4). During transient hyperperfusion and chronic hypoperfusion stages, ^{123}I-iodoamphetamine FLAIR demonstrated marked cortical edema and chronic atrophic change of the affected region, respectively. Subtle diffusion weighted imaging hyperintensity in the affected area was shown between PODs 1 and 7 but disappeared on

POD 35, despite slowly progressive neuronal death documented on ^{123}I-IMZ in the subacute phase (PODs 18–55), during which T1 cortical hyperintensity became prominent (PODs 35–56). The hyperperfusion state of the affected cortex was also confirmed by ^{123}I-IMP SPECT on POD 12. Hyperperfusion of the affected cortex gradually improved and returned to normal, as shown by ^{123}I-IMP SPECT on POD 53. Follow-up MR images showed unique chronological changes such that cortical hyperintensity of the affected cortex appeared on POD 35 and persisted at least until POD 56. Of note, cortical hyperintensity on FLAIR peaked on POD 7 and then gradually decreased in intensity and appeared almost normal on POD 56. In the late chronic stage on POD 237, cortical atrophy with secondary degeneration of the underlying subcortical white matter was noted. No hemorrhagic transformation was noted in the affected regions on CT scans throughout the observation period.

Follow-Up. The patient's cranial nerve III palsy and restlessness gradually improved and he resumed his previous lifestyle 5 months after the second surgery. Eight months after surgery, his Mini-Mental State Examination status returned to normal.

Discussion

We have presented, for the first time, dynamic neuropathological correlations between slowly progressive neuronal death during postischemic hyperperfusion, as shown on ^{123}I-IMZ and ^{123}I-IMP SPECT scans, and emerging cortical laminar necrosis, as shown on T1-weighted MR images, after RA/ECA-MCA bypass grafting for an intracavernous CA aneurysm.

Intracavernous CA aneurysms are usually treated by trapping with/without EC-IC bypass based on presumed tolerance to CA sacrifice.[9] If the CA does not tolerate the balloon test occlusion, a high-flow bypass is indicated when CA sacrifice is performed. Creation of an RA/ECA-MCA bypass graft is a common method of high-flow bypass, and the technical standards and pitfalls have been reported previously.[9,12] The incidence of ischemic complications has been reported to be ~ 10%[9] as a result of early graft occlusion and other causes, but the underlying etiological force, most of which has been considered thromboembolic, remains unproven in most cases.[6,9]

Cortical laminar necrosis is a permanent brain injury characterized on T1-weighted MR images by high-intensity cortical lesions that follow the gyral anatomy of the cerebral cortex. Histopathological and experimental animal studies have demonstrated much more vulnerability of the gray matter than white matter to ischemic necrosis due to hypoperfusion.[19] Previous studies have reported characteristic MR imaging findings of cortical laminar necrosis caused by hypoxic or ischemic brain damage.[7,19] Cortical enhancement on postcontrast T1-weighted images in the subacute stage, suggesting breakdown of the blood-brain barrier, and hyperintense cortical lesions on unenhanced T1-weighted images during the late subacute and early chronic stages were reported to be distributed in the laminae. Cortical laminar necrosis is usually reported
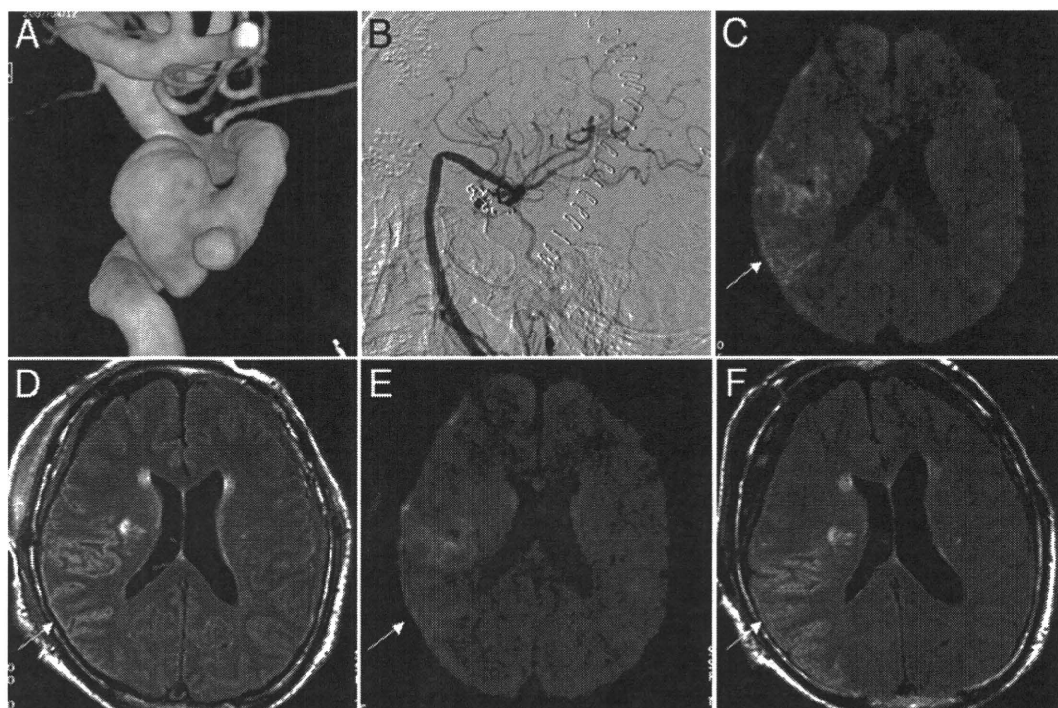
Fig. 1. **A:** Three-dimensional rotational CA angiogram showing a large intracavernous aneurysm that was treated with radial artery/ECA-MCA bypass grafting. **B:** Postoperative angiogram. **C and D:** Diffusion weighted **(C)** and FLAIR **(D)** images obtained on POD 1, showing only subtle hyperintensity in the right temporal cortex subjected to temporary clipping. **E and F:** Diffusion weighted **(E)** and FLAIR **(F)** images obtained on POD 7 when the patient became restless. Both of the hyperintensities following a gyral pattern appear slightly increased and well demarcated. *Arrows* indicate the affected region in the temporal lobe.

to be associated with volume loss of the affected cortex in the chronic stage.[20] Weiller and coworkers[20] have reported finding atrophy of the opercular cortex overlying the subcortical infarct on follow-up MR images ~ 1 year after the insult, suggesting that neuronal loss progresses over time.[13,20] In the present case we observed similar chronological changes of MR imaging signals on T1-weighted and FLAIR images and clearly illustrated the dynamic process of slowly progressive neuronal death associated with postischemic hyperperfusion in the affected cortex, where cortical hyperintensity was emerging in the subacute phase, following subtle diffusion weighted imaging–documented abnormalities in the acute phase.

Hyperperfusion is defined as a significant increase in cerebral blood flow relative to the homologous area of the contralateral hemisphere,[10] and it is known to occur after carotid endarterectomy, EC-IC bypass, and giant aneurysm clipping in patients with chronically impaired cerebrovascular reserve. Previous studies that involved the use of PET or SPECT scanning suggest that hyperperfusion may sometimes be associated with incomplete infarction or selective neuronal loss.[3,13] Flumazenil and ^{123}I-IMZ are markers of central benzodiazepine receptors, part of the GABAergic complex,[2] and ideal markers of periinfarct tissue and incomplete brain infarcts.[16] Sette et al.[16] have reported marked hyperperfusion in the affected territory in ischemic stroke, together with mildly reduced binding of ^{11}C-flumazenil in the acute stage, followed by reduced ^{11}C-flumazenil binding and reduced cerebral metabolic rates of glucose despite unaltered MR imaging findings

in the subacute stage. Nakagawara and colleagues[13] have also reported using ^{123}I-IMZ SPECT in 2 patients with extensive hyperperfusion in the acute stage who exhibited reduced binding of ^{123}I-iomazenil in these areas in the chronic stage despite normal CT findings. The degree and duration of moderate ischemia in the present case was probably in the narrow range, which caused slowly progressive neuronal death without the development of frank infarction involving subcortical white matter, as reported in transient ischemia in animal models.[1] In internal carotid artery occlusive disease, selective neuronal damage was reported to occur beyond the regions of infarcts by hemodynamic ischemia in the chronic stage, as demonstrated on ^{11}C-flumazenil PET scans.[22]

The diagnostic significance of diffusion weighted imaging deserves some mention. Diffusion weighted imaging is considered an accurate predictor of the extent of infarction during the acute or early subacute phase of cerebral ischemia. Heiss et al.[4] compared the probability of cortical infarction by examining flumazenil binding on PET and diffusion weighted images in early ischemic stroke; they concluded that these modalities are comparable in predicting the probability of ischemic cortical infarction. Benzodiazepine receptor activity is a reliable marker of neuronal integrity in the cortex, but movement of water molecules in the extracellular space may be a more variable indicator of tissue damage, such that the false-positive volumes not included in the final infarct were larger for diffusion weighted imaging.[4] Subtle cortical hyperintensity on diffusion weighted imaging of the

34